Galápagos hydroclimate of the Common Era from paired microalgal and mangrove biomarker $^{2}H/^{1}H$ values

Daniel B. Nelson[a,1,2] and Julian P. Sachs[a]

[a]School of Oceanography, University of Washington, Seattle, WA 98195

Edited by Katherine H. Freeman, Pennsylvania State University, University Park, PA, and approved February 5, 2016 (received for review August 15, 2015)

Tropical maritime precipitation affects global atmospheric circulation, influencing storm tracks and the size and location of subtropical deserts. Paleoclimate evidence suggests centuries-long changes in rainfall in the tropical Pacific over the past 2,000 y, but these remain poorly characterized across most of the ocean where long, continuous proxy records capable of resolving decadal-to-centennial climate changes are still virtually nonexistent despite substantial efforts to develop them. Here we apply a new climate proxy based on paired hydrogen isotope ratios from microalgal and mangrove-derived sedimentary lipids in the Galápagos to reconstruct maritime precipitation changes during the Common Era. We show that increased rainfall during the Little Ice Age (LIA) (~1400–1850 CE) was likely caused by a southward migration of the Intertropical Convergence Zone (ITCZ), and that this shift occurred later than previously recognized, coeval with dynamically linked precipitation changes in South America and the western tropical Pacific. Before the LIA, we show that drier conditions at the onset of the Medieval Warm Period (~800–1300 CE) and wetter conditions *ca*. 2 ka were caused by changes in the El Niño/Southern Oscillation (ENSO). Collectively, the large natural variations in tropical rainfall we detect, each linked to a multicentury perturbation of either ENSO-like variability or the ITCZ, imply a high sensitivity of tropical Pacific rainfall to climate forcings.

paleoclimate | hydrogen isotopes | tropical Pacific | ENSO | ITCZ

Tropical Pacific precipitation patterns have a profound impact on global climate, and changes are projected far outside the region of origin (1). Coherent understanding of these climate dynamics is therefore critical for understanding when and how the distribution and intensity of global precipitation patterns have changed in the past and will change in the future, with far-reaching implications for managing the demand for freshwater resources in major population and agricultural centers in the tropics and midlatitudes. Tropical Pacific precipitation is largely dominated by zonally asymmetric variability associated with El Niño/Southern Oscillation (ENSO) and the zonally symmetric annual north–south migration of the Intertropical Convergence Zone (ITCZ). The extensive geographic footprint and intensity of these phenomena suggests that capturing their evolution in the paleoclimate record and within Earth system models should be straightforward, but in practice these targets have proven elusive. Perennial problems persist in simulating realistic ITCZ and ENSO dynamics, even in the latest generation of state-of-the-art climate models (2, 3). Paleoclimate records should theoretically be able to help constrain some of these dynamics, but it is challenging to distinguish between ITCZ- and ENSO-driven changes in a record from a single location because rainfall alone is influenced by both phenomena (4–8). Networks of paleoclimate records can help to resolve these issues, but proxy archives that are within the core ITCZ and ENSO regions (i.e., at sea level in the tropical Pacific) and have both the temporal resolution and duration to record the decadal to centennial changes that are of greatest societal relevance have been difficult to obtain.

The Galápagos archipelago in the eastern equatorial Pacific is in a key center of action for ENSO and is ideally located for testing hypotheses regarding changes in the southern extent of annual ITCZ migration (7, 9). Precipitation is highly variable on seasonal and interannual timescales and correlated with the Niño 1–4 indices (Fig. 1 and Fig. S1) as well as with the multivariate ENSO index, local sea surface temperature, and the isotopic composition of precipitation (4, 5, 10). El Niño events bring heavy rain to the Galápagos, and changes in their intensity or recurrence interval manifest in the local precipitation record, but with increased sensitivity to eastern Pacific, as opposed to central Pacific, El Niño events (Fig. S1) (4). The islands are at the modern southernmost extent of annual ITCZ migration, and changes in its maximum southerly range bring large increases in annual rainfall (Fig. 1).

The $\delta^{2}H$ value of tropical precipitation as it falls and is temporarily sequestered in lakes ($\delta^{2}H_{Water}$) reflects its transport history, making $\delta^{2}H_{Water}$ values an excellent hydroclimate proxy (11). Photoautotrophic organisms use hydrogen from these waters to synthesize lipids, transforming $\delta^{2}H_{Water}$ values into lipid $\delta^{2}H$ values ($\delta^{2}H_{Lipid}$) that are preserved in sediments over geologic time. However, $\delta^{2}H_{Lipid}$ values are offset from $\delta^{2}H_{Water}$ values by isotopic fractionation that occurs during biosynthesis and that varies by organism, and in response to environmental conditions such as salinity (12). This complicates efforts to apply $\delta^{2}H_{Lipid}$ values as paleoclimate proxies in coastal sediments where salinity varies over time and common biomarkers are synthesized by a wide variety of organisms. Mangrove trees and cyanobacteria living in these locations access common source water, but salinity has an opposing effect on $^{2}H/^{1}H$ fractionation expressed in their lipids (13–15). In phytoplankton $^{2}H/^{1}H$ fractionation decreases by 0.7–2.0‰ per unit increase in salinity (14, 15), whereas in mangroves

Significance

The equatorial Pacific is centrally important in Earth's climate system. Changes there cause disruptions to global economies and food and water security. Yet, projected tropical precipitation changes in response to higher greenhouse gas concentrations remain uncertain, due in part to a scarcity of paleoclimate records to validate models. We therefore applied a new method in Galápagos lakes for reconstructing rainfall and salinity using sedimentary lipids from microalgae and mangrove trees. Our data revise the understanding of changes over the Common Era to provide a spatially and temporally coherent view of tropical Pacific rainfall. We separate convergence zone from El Niño-driven changes and observe substantial fluctuations even in the absence of perturbations as large as current anthropogenic forcing.

Author contributions: D.B.N. and J.P.S. designed research; D.B.N. performed research; D.B.N. analyzed data; and D.B.N. and J.P.S. wrote the paper.

The authors declare no conflict of interest.

This article is a PNAS Direct Submission.

[1]To whom correspondence should be addressed. Email: daniel.nelson@unibas.ch.

[2]Present address: Department of Environmental Sciences – Botany, University of Basel, 4056 Basel, Switzerland.

This article contains supporting information online at www.pnas.org/lookup/suppl/doi:10.1073/pnas.1516271113/-/DCSupplemental.

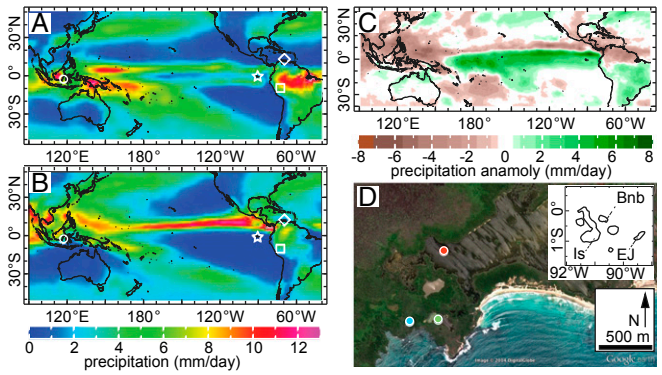

Fig. 1. Precipitation data and base map for Isabela lakes. (*A*) Average wet- (February–April) and (*B*) dry-season (August–October) precipitation (1997–2008; NASA GPCP). Locations: Galápagos (star), Cariaco Basin (diamond), Lake Pumacocha (square), Makassar Straight (circle). (*C*) Niño1+2 precipitation anomaly shows influence of eastern Pacific El Niño and La Niña events on Galápagos precipitation. Anomalies in figure are the difference between years where Niño 1+2 > 1 °C and years where Niño 1+2 < 1 °C (dataset from *A* and *B*). Comparison between Niño 1+2 and Niño 3.4 is shown in Fig. S1. (*D*) Map shows locations of Isabela Island lakes within the Galápagos archipelago (Map data: Google, DigitalGlobe) and coring locations in each lake (Diablas, red; Verdes, green; Escondida, blue). Bnb, Bainbridge Crater; EJ, El Junco Lake; Is, Isabela lakes.

it increases by 0.7–1.7‰ (13, 16). Combining these calibrations with measured algal and mangrove δ^2H_{Lipid} values provides a method to simultaneously and quantitatively reconstruct salinity and δ^2H_{Water} values. This approach circumvents shortcomings that have previously hindered even qualitative application of δ^2H_{Lipid} values in these environments and opens the door for widespread application of this technique in the high-accumulation-rate saline coastal lakes that are common in the tropics. This newly developed paired biomarker approach was applied to sediments collected from three coastal saline ponds on Isabela Island in the Galápagos archipelago (Fig. 1) to reconstruct salinity and δ^2H_{Water} values spanning the past 2,000 y of the Common Era.

Results and Discussion

Site Characterization and Sedimentology. Surface water δ^2H values were 13‰, 10‰, and 4‰ for Poza de las Diablas, Pozas Verdes, and Poza Escondida, respectively, with corresponding $\delta^{18}O$ values of 2.4‰, 2.6‰, and 0.9‰. Although the water level in each of these systems changes daily with the tides, indicating active connections to the sea, the modern salinities in Poza de las Diablas (7 $g{\cdot}L^{-1}$), Poza Escondida (33 $g{\cdot}L^{-1}$), and Pozas Verdes (44 $g{\cdot}L^{-1}$) indicate variable inputs of freshwater and seawater as well as degrees of evaporative enrichment.

Poza de las Diablas sediments were pink cyanobacterial deposits and contained few lithological changes between the sediment–water interface and ∼340-cm depth (Fig. S2). Sediments from Poza Escondida were mangrove peat throughout the entire 83-cm recovered sequence. Pozas Verdes surface sediments were light tan in color and composed of gelatinous material with minimal sedimentary structure to a depth of ∼50 cm, below which sediments transitioned to mangrove peat.

Chronological uncertainty varied due to combined analytical and calibration errors but averaged 36 ± 16 y for all sediment samples in all lakes based on Monte Carlo simulations (*Supporting Information*).

Biomarkers. The biomarker distribution in Poza de las Diablas sediments primarily included nC_{24}-alkanol and compounds that were tentatively identified as glycolipids based on comparison with published mass spectra from Ace Lake, Antarctica sediments (17) and also as described from Lake Malawi (18). The nC_{24}-alkanol in Diablas sediment was interpreted as a degradation product of the glycolipids and used as a cyanobacterial marker in this system, based on interpretation of ion fragments in the glycolipid mass spectra and the relationships described from Ace Lake (*Supporting Information*) (17). Taraxerol was used as a biomarker for *Rhizophora* mangroves in the Diablas, Verdes, and Escondida catchments (19). In this location these mangroves are the sole source of this triterpenoid, making it much more specific than more commonly used higher plant leaf wax *n*-alkanes and *n*-alkanoic acids that are produced by all vascular plants. Dinosterol, a dinoflagellate biomarker (20), was used as a secondary algal compound.

Poza de las Diablas δ^2H_{Dino}, δ^2H_{Tarax}, and δ^2H_{C24OL} values show generally consistent patterns, with negative trends from 1350–1850 CE, positive trends after 1800 CE, and average δ^2H values that are 7–9‰ more depleted between 1600–1850 CE than those from after 1900 CE (Fig. 2 and Fig. S3). Field survey data show that salinity effects dominate over other factors for algal lipids at global scale (15), but changes in temperature, humidity, growth rate, and biological sources can also alter $^2H/^1H$ fractionation in algae and higher plants (12, 21, 22). However, temperature and humidity changes at sea level are likely to have been small in the Galápagos given limited modern seasonal and interannual changes compared with precipitation (*Supporting Information* and Table S1) (23). High relative humidity also limits the impact of transpiration on δ^2H_{Tarax} values (24). Variable biological sources are unlikely to be a factor given the source specificity of the targeted biomarkers. Additional factors, such as nutrient or light-induced growth rate changes, would not be expected to similarly influence all lipid producers, leaving changing δ^2H_{Water} values as the most probable remaining mechanism to explain temporal changes in lipid δ^2H values in Poza de las Diablas.

Taraxerol and dinosterol δ^2H values from Poza Escondida and Pozas Verdes share the major features described in the Poza de las Diablas δ^2H values, with the exception of post-1800 CE Pozas Verdes taraxerol values, which were highly variable (Fig. 2 and Fig. S3). This may indicate increased importance of salinity

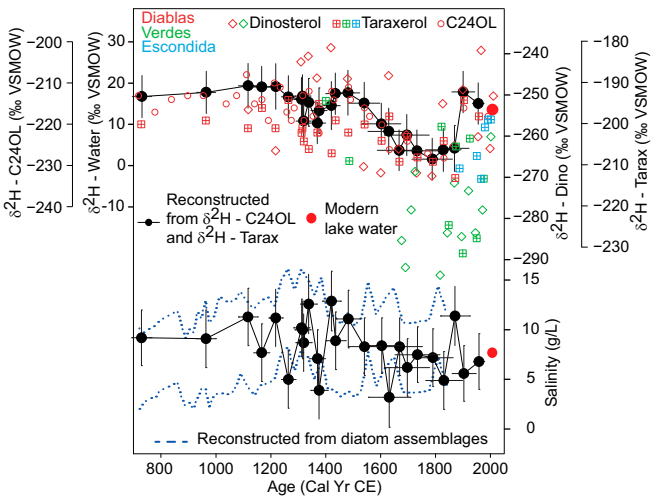

Fig. 2. δ^2H_{Water} (black, top) and salinity (black, bottom) from ∼700–2008 CE reconstructed from Poza de las Diablas δ^2H_{Tarax} and δ^2H_{C24OL} measurements (red solid circles are measured lake water). Error bars are 1 SD of Monte Carlo simulations and include age-model, analytical, algal-, and mangrove-biomarker salinity fractionation sensitivity uncertainties. Error limits of diatom-derived salinity reconstruction (25) are shown (bottom, dashed blue lines), but that time series is omitted here for clarity. Additional colored symbols (top) show all biomarker δ^2H data for the time interval displayed: nC_{24OL} (open circles), dinosterol (diamonds), and taraxerol (crossed squares) from Poza de las Diablas (red), Pozas Verdes (green), and Poza Escondida (blue).

changes in this lake, which receives limited freshwater input as evidenced by modern hypersaline conditions.

Lake-Water Isotope and Salinity Reconstructions. δ^2H_{Tarax} and δ^2H_{C24OL} values were used to calculate original source water salinity and δ^2H_{Water} values by combining the definition of the fractionation factor, $\alpha = (\delta^2H_{Lipid} + 1)/(\delta^2H_{Water} + 1)$, with α – salinity calibrations for each lipid to describe paired systems that were solved directly. Specifically, $m_{Tarax} * \text{salinity} + b_{Tarax} = (\delta^2H_{Tarax} + 1)/(\delta^2H_{Water} + 1)$, and $m_{C24OL} * \text{salinity} + b_{C24OL} = (\delta^2H_{C24OL} + 1)/(\delta^2H_{Water} + 1)$, where m and b are the respective slope and intercept for each lipid calibration. Monte Carlo simulations were used to quantify uncertainties arising from the measurements as well as the calibrations (Fig. 2). Comparison of this reconstruction with an independent diatom-based salinity record from different sediment cores from the same lake shows that both are entirely overlapping within their respective uncertainties and indicates maximum salinities of about 12 g·L^{-1} *ca.* 1400 CE (Figs. 2 and 3) (25). This effectively cross-validates both methods and supports the fidelity of the new δ^2H_{Water} record.

Reconstructed Lake-Water Changes and Mechanisms. The combined 2,000-y salinity record (Figs. 3 and 4) decreases from 14.3 ± 4.0 to 5.8 ± 4.0 g·L^{-1} from 100 to 600 CE, then increases to 12.9 ± 3.0 g·L^{-1} by 1400 CE, and finally decreases to reach measured values in June 2008 of 7.4 g·L^{-1}. δ^2H_{Water} values increased from –9.8 ± 8.9 to 17.5 ± 8.9‰ between 0 and 700 CE, where they remained elevated until declining from 19.1 ± 5.5 to 10.3 ± 5.0‰ between 1200 and 1350 CE, followed by an increase to 17.6 ± 5.4‰ by 1500 CE, a drop to 1.6 ± 5.0‰ at 1800 CE, and a final increase to the June 2008 value of 13.5‰ (Figs. 3 and 4).

The most striking features of the salinity and δ^2H_{Water} records are the prolonged opposing trends before the Little Ice Age (LIA), which are difficult to explain in the context of changing precipitation balance alone, because wetter or drier conditions would be expected to cause concurrent decreases or increases. Changing El Niño frequency, intensity, or centennial-scale mean state shifts are mechanisms that would allow for these patterns to coexist. Although chronological uncertainty prevents distinguishing between these, all would explain the observations because El Niño events are associated with increased precipitation and lowered δ^2H values (4, 5) as well as increases in sea level of up to 400 mm in the Galápagos (26). Conversely, reduced El Niño activity would cause reduced fluxes of both seawater and precipitation to the lake, higher δ^2H values of precipitation and runoff, and increased evaporative enrichment of the lake water. The opposing salinity and δ^2H_{Water} trends are therefore interpreted as periods when ENSO-like variability was the dominant control on precipitation in the eastern equatorial Pacific. Intervals where δ^2H_{Water} changes occur without opposing shifts in salinity require another mechanism, which is provided by differences in rainfall associated with additional impacts of changes in ITCZ latitude. This would alter precipitation patterns, but the passage of the ITCZ is not associated with large modifications in sea level (27). This interpretation was evaluated using a mass balance model to confirm that reconstructed salinity and δ^2H_{Water} values are attainable with realistic variations in precipitation and seawater influx alone (*Supporting Information* and Table S2).

Other Factors Affecting Seawater Connectivity. In addition to the relationship between climate and lake-water chemistry, changes in coastal geomorphology, island subsidence, seismic uplift events, sediment accumulation in the lake, and eustatic sea level also have the potential to affect the difference in elevation between the lake floor and local sea level. However, in considering the likely impact of each of these factors on the sediments, none can as plausibly explain the divergent relationship between salinity and δ^2H_{Water} values, or the centennial and shorter-scale variability in the

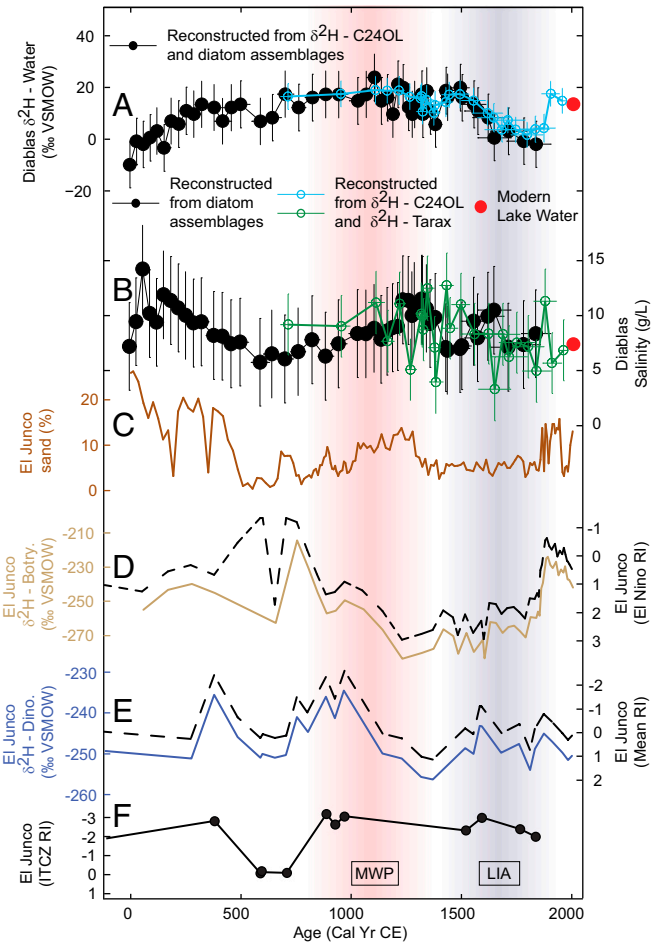

Fig. 3. Selected Galápagos sediment records from ~0 to 2008 CE. (*A*) Poza de las Diablas δ^2H_{Water} and (*B*) salinity reconstructions from δ^2H_{Tarax} and δ^2H_{C24OL} (blue and green) compared with δ^2H_{Water} values (black) calculated from the diatom-salinity record (25) and δ^2H_{C24OL} values, and the diatom-salinity reconstruction (black). Red circles are measured lake water. Errors are 1 SD of Monte Carlo, or as published for the diatom salinity reconstruction. (*C*) El Junco Lake percent sand (5). (*D*) El Junco botryococcene δ^2H values (7, 8) and calculated El Junco El Niño rainfall index (4). (*E*) El Junco dinosterol δ^2H values and calculated El Junco mean rainfall index (4). (*F*) Calculated El Junco ITCZ rainfall index (4). Medieval Warm Period (MWP) and LIA periods indicated with red and blue shading, respectively.

reconstructions. If coastal processes caused significant seawater incursions, or if seismic uplift events occurred, these would likely have resulted in step changes in the sediment character and deposition rates and caused disconformities. Abrupt changes in sediment lithology did occur in Poza Diablas sediments before 2 ka, suggesting possible tectonic or morphological changes before this time, and as a consequence the hydroclimate reconstructions are not extended further despite the fact that the sediment sequence is much longer. After 2 ka no lithological disturbances were observed (Fig. S2) even though large uplift events have occurred in other areas of the Galápagos in recorded history, including the 4.5-m uplift in Urvina Bay in 1954 (28). The Poza de las Diablas sector of Isabela Island is subsiding at ~0.46 mm·y^{-1} (29), but average sedimentation rates over the past 2,000 y have been 1.7·mm y^{-1}, and modeled eustatic sea level has steadily declined 0.075 mm·y^{-1} over the same interval (25). Combining these processes yields an estimated lake floor to sea level difference *ca.* 2 ka that was 2.6 m smaller than the modern difference. However, these potential nonclimate mechanisms for altering the seawater connection are unidirectional, and therefore they cannot account

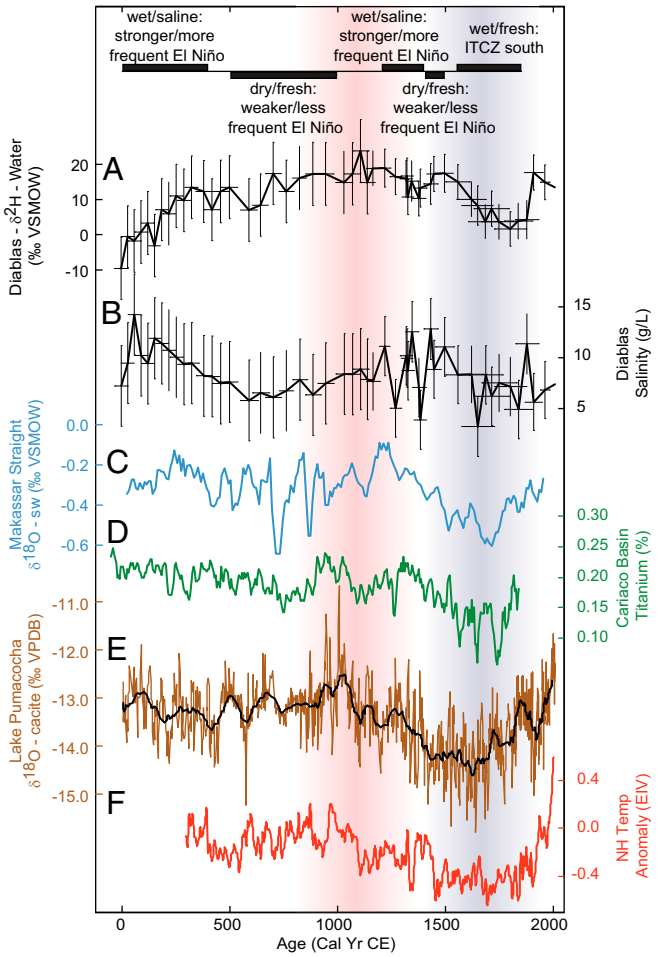

Fig. 4. Comparison of Poza de las Diablas hydroclimate reconstructions with regional paleoclimate records (error bars are as in previous figures). (*A*) δ^2H_{Water} and (*B*) salinity reconstructions from Poza de las Diablas after combining the biomarker isotope, diatom, and measured lake-water values. (*C*) Seawater $\delta^{18}O$ values from the Makassar Straight (37). (*D*) Cariaco Basin % titanium (9). (*E*) Lake Pumacocha sedimentary calcite $\delta^{18}O$ values (31) with running 30-y smooth. (*F*) Northern Hemisphere temperature reconstruction (36). MWP and LIA periods indicated with red and blue shading, respectively.

for decadal and centennial-scale fluctuations in both signals, and they also do not explain the divergent salinity and δ^2H_{Water} values.

Galápagos Hydroclimate of the Common Era. Following the interpretation framework based on sea level and precipitation changes, the major features of the reconstructed salinity and δ^2H_{Water} values from Poza de las Diablas before ~1550 CE are interpreted in the context of a dominant role for ENSO-like patterns. Compared with adjacent time intervals, low δ^2H_{Water} values (Figs. 3*A* and 4*A*) and high salinity (Figs. 3*B* and 4*B*) from ~0–400 CE and ~1200–1400 CE are taken to indicate stronger or more frequent El Niño events or a more El Niño-like mean state. Low salinity with high δ^2H_{Water} values from ~500–1000 CE, and decreasing salinity with increasing δ^2H_{Water} values from ~1400–1500 CE are interpreted to indicate drier conditions resulting in reduced El Niño-like conditions. Declining δ^2H_{Water} values occurred without synchronous salinity increases from ~1550–1850 CE, suggesting added impacts from the ITCZ (*Supporting Information* and Table S2).

The Poza de las Diablas data provide a critical compliment to existing Galápagos hydroclimate records from the last 2,000 y, in particular to a number of records from El Junco Lake in the highlands of San Cristobal Island (Fig. 1). Diablas age model uncertainty averages ~40 y, and is similar to that from El Junco (8). As a consequence, comparisons between these and other sites are limited to centennial scale. The major features of the Poza de las Diablas record before ~1550 CE (Fig. 3 *A* and *B*) are consistent with ENSO changes identified from El Junco sand content (5) (Fig. 3*C*), δ^2H values of botryococcene lipids (Fig. 3*D*) (7, 8), and δ^2H values of dinosterol (4) (Fig. 3*E*). These ENSO patterns are also consistent with interpretations of sediment lithology changes identified from Bainbridge Crater (6).

Evidence for wetter conditions at Poza de las Diablas in response to ITCZ changes from 1550–1850 CE are less consistent with other records in the Galápagos. Rainfall indices (Fig. 3 *D*–*F*) calculated from El Junco biomarker δ^2H data do not indicate an ITCZ response (4) despite the fact that lower botryococcene δ^2H values from El Junco beginning as early as 750 CE were previously interpreted as evidence for a southward ITCZ shift (7). The El Junco sand record also displays few changes after ~1550 CE apart from the anthropogenic disturbances near the core top (Fig. 3*C*) (5). The apparent discrepancies suggest differences in climate between the highlands and lowlands. At the 670-m elevation of El Junco Lake, for reasons that are not well understood, Galápagos highlands receive the majority of annual precipitation as frequent light rains in the cool season when the ITCZ is furthest north and the lowlands remain dry (23). Highland sites also receive 26 ± 16% of cool season rainfall from direct cloud water interception associated with *garua* fog (30). Changes to the intensity and or distribution of either of these moisture sources may have altered the hydrologic balance of El Junco in ways that did not manifest equally in the sand and biomarker isotope records and may have caused an earlier onset of wetter conditions (Fig. 3 *C* and *D*). In contrast, lowland sites are not affected by these complexities and may therefore serve as better locations to detect canonical ITCZ precipitation patterns.

Regional Significance of Observed Changes. The later onset of wetter conditions and shorter duration of the LIA response detected at Poza de las Diablas compared with El Junco agrees more closely with the timing and duration of the southward ITCZ shift identified in titanium concentrations in the Cariaco Basin (9) (Fig. 4*D*). Increased South American summer monsoon precipitation associated with the LIA ITCZ changes inferred from sedimentary calcite $\delta^{18}O$ values (31) also demonstrate the direct regional temporal coherence of this response (Fig. 4*E*), as do cave and terrestrial runoff records (32, 33). This interpretation is consistent with dynamical arguments that the mean ITCZ latitude is regulated by the meridional temperature gradient (34, 35), with lowest northern hemisphere temperatures of the last 1.7 thousand years occurring in the core LIA *ca*. 1650–1750 CE (36) (Fig. 4*F*), coincident with changing δ^2H_{water} values in Poza de las Diablas. Western Pacific seawater $\delta^{18}O$ values were also low in the Makassar Straight in Indonesia within the primary LIA interval, indicating wetter conditions (37) (Fig. 4*C*) and basin-wide zonal precipitation symmetry, consistent with an ITCZ mechanism. This record also offers additional support for the proposed ENSO-like patterns identified in Poza de las Diablas through opposing, zonally asymmetric changes in water isotope values that imply drier conditions from ~0 to 400 CE when Diablas was wet, wetter conditions from ~500–1000 CE when Diablas was dry, and drier conditions from ~1200–1400 CE when Diablas was wet (Fig. 4 *A*–*C*).

Conclusion

Applied here for the first time to our knowledge are new hydroclimate proxies based on δ^2H values of paired microalgal and mangrove-biomarkers tailored to high-accumulation-rate saline coastal lakes that are common in the tropics. The data are in broad agreement with previous results but offer several

ENVIRONMENTAL SCIENCES

important insights on tropical hydroclimate over the Common Era. The data confirm that maritime precipitation increased during the LIA and are consistent with a southward ITCZ shift but also reconcile the timing of these changes to show temporal synchronicity across the Pacific. The data also show that before the LIA, ENSO-like mechanisms were more important than the ITCZ in regulating decadal-to-centennial-scale maritime rainfall patterns in the eastern tropical Pacific, highlighting the unique nature of the LIA in the context of the past 2,000 y, and confirming the capacity for multidecadal and longer timescale changes in ENSO-like variability. This provides an important complement to sub-annually resolved reconstructions from short-lived corals (38) or mollusks (39) that are ideally suited for detecting changes in ENSO variance but lack the continuous duration to assess long timescales. The centennial-scale changes in both ENSO mean state and ITCZ dynamics that characterized the last 2,000 y highlight the importance of adequately capturing these climate modes in future climate projections forced by a radiative perturbation far in excess of any that occurred in the last 2,000 y.

Materials and Methods

Sample Collection. Sediment cores were collected from the lakes on southern Isabela Island in June 2008 with a universal corer (Aquatic Research) and a Livingstone-type piston corer (Geo-Core). Surface cores were sectioned in the field at 1-cm intervals, and remaining cores were split longitudinally after transport to the University of Washington. In total, an 8.79-m continuous sediment sequence was recovered from Poza de las Diablas, 5.4 m from Pozas Verdes, and 83 cm from Poza Escondida. Lake water was filtered onto combusted 0.7-μm-pore-size glass fiber filters and aquatic and terrestrial vegetation samples were collected to aid in the interpretation of down-core geochemical data. Surface water isotope samples were also collected from each lake and analyzed at Georgia Institute of Technology in the laboratory of Kim Cobb by cavity ring-down spectroscopy with a Picarro water isotope analyzer (Picarro Inc.) using standard methods. Lake-water temperature, pH, conductivity, salinity, and temperature were recorded on-site using a portable data sonde (Geo Scientific Ltd.).

Sediment Age Control. Sediment cores were split, photographed, and described at the University of Washington. Terrestrial macrofossils and bulk sediment total organic carbon were used for radiocarbon dating (Fig. S4 and Table S3). Samples were sent to the Xi'an Accelerator Mass Spectrometry Centre at the Institute of Earth Environment, Chinese Academy of Sciences, or to Direct AMS. Samples analyzed by Direct AMS were pretreated at the University of Washington following an acid–base–acid procedure (40), whereas samples sent to the Xi'an laboratory were pretreated at that facility. Radiocarbon ages were calibrated using SH13 (41) and the bomb curve extension (42) in Calib 7.0 (43). Age-depth models were constructed for each lake using the median calibrated age and applying a monotone piecewise cubic interpolation function (44). Chronological uncertainty was assessed using Monte Carlo simulations to generate 1,000 realizations of alternative age-depth models for each lake that incorporate the non-Gaussian probability density function of each calibrated radiocarbon age (45).

Biomarker Analyses. Subsamples (1 to 2 cm thick) were removed from split cores or from sectioned material for lipid analyses. Samples were transferred to combusted glass vials, frozen, and then freeze-dried. Dry material was extracted in 9:1 dichloromethane and methanol (MeOH) on an accelerated solvent extractor (ASE) 200 (Dionex). Before extraction, nC$_{21}$-alcohol (1-heneicosanol), nC$_{21}$-acid (heneicosanoic acid), and nC$_{36}$-alkane (hexatriacontane) quantification/recovery standards were added. The ASE was operated at 100 °C and 1,500 psi with three 5-min static phases. Solvent was evaporated under N_2 from the total lipid extract (TLE) (Turbo-vap; Caliper). After an initial set of 45 samples was analyzed, 20 additional samples were extracted following a modified protocol that included saponification of the TLE to improve compound yield. Saponification was performed using 1 N potassium hydroxide in MeOH and Nanopure water (Barnstead Nanopure Infinity water system; Thermo-Fisher) at 70 °C overnight. The saponified TLE was acidified to pH ∼2 with HCl, recovered from the aqueous MeOH using hexane liquid–liquid extractions, rinsed once with Nanopure water, and dried over sodium sulfate.

Alcohol and polar fractions were isolated with column chromatography following published methods (15, 46). Biomarkers were identified from subsamples that were either silylated [20 μL N,O-bis(trimethylsilyl)trifluoroacetamide and 20 μL pyridine, at 60 °C for 60 min] or acetylated (20 μL acetic anhydride and 20 μL pyridine, at 70 °C for 30 min). The derivatized aliquots were evaporated to dryness under N_2 and dissolved in toluene, and a 5α-cholestane quantification standard was added to the samples before analysis by GC-MS. Samples were injected in splitless mode at 300 °C using helium carrier gas at 1.5 mL/min on an Agilent 6890N GC with 5975 inert mass selective detector equipped with an Agilent (formerly Varian) VF-17ms column (60 m × 0.32 mm × 0.25 μm). The oven program began at 110 °C for sample injection, then increased to 170 °C at 15 °C/min, then to 325 °C at 5 °C/min and held for 24 min. Alcohol fractions were acetylated and analyzed by GC-MS following the same procedure and compounds were identified by comparison with literature. Subsamples of acetylated alcohol fractions were taken for later hydrogen isotope analysis of the compounds present at highest abundance. Alcohol fractions that contained dinosterol (4α, 23, 24-trimethyl-5α-cholest-22E-en-3β-ol), and some that contained taraxerol (3β-D-friedoolean-14-en-3-ol), were further purified using HPLC-MS following published methods (46).

The δ^2H values of acetylated dinosterol and taraxerol were analyzed following published methods (46). nC$_{24}$-alkanol (1-tetracosanol) δ^2H values were analyzed similarly, but for these the GC oven was held at an initial temperature of 120 °C for 10 min, then increased to 325 °C at 8 °C/min and held for 15 min. All measurements were corrected for the hydrogen added during acetylation following published methods (15). An overall analytical uncertainty for each compound was calculated from the pooled uncertainty of replicate analyses conducted across multiple days in most cases (47). These were 4.0‰, 4.4‰, and 4.8‰ for dinosterol, taraxerol, and C$_{24}$ n-alkanol from Poza de las Diablas; 4.4‰ and 5.1‰ for dinosterol and taraxerol from Pozas Verdes; and 4.7‰ for taraxerol from Poza Escondida (Fig. S3 and Dataset S1).

Salinity and Water δ^2H_{water} Reconstructions. The opposing salinity sensitivities but common δ^2H_{Water} responses for microalgal and mangrove lipids were used to calculate down-core salinity and δ^2H_{Water} values from Poza de las Diablas sediments for the past ∼1,350 y using taraxerol (δ^2H_{Tarax}) and nC$_{24}$-alkanol (δ^2H_{C24OL}) values (Fig. 2, Fig. S3, and Dataset S1). Specific or sufficiently detailed salinity calibrations for each compound are unavailable, so these relationships were established by combining literature values with measurements from the modern environment. A range of salinity sensitivities for $^2H/^1H$ fractionation was applied for each compound that encompass those from existing studies of similar compounds, or 0.4‰ to 2.2‰ for algae and −0.7‰ to −1.7‰ for mangroves (13–16, 46, 48, 49). These were combined with core-top sediment lipid values and measured lake-water salinity and δ^2H values to calculate a regression equation for the sensitivity of biosynthetic $^2H/^1H$ fractionation to salinity for each compound. Monte Carlo simulations (n = 1,000) were used to account for calibration uncertainty, as well as the analytical uncertainty in the lipid δ^2H values, and the calibrated radiocarbon ages (45). Although alkenone batch cultures from pelagic species have suggested greater salinity sensitivity for $^2H/^1H$ fractionation than our assumed range (50), no similarly large effect has been observed in coastal or inland species or samples, and there is debate about the use of hydrogen isotope values from multiple compound C$_{37}$ alkenone chromatographic peaks, as well as the use of batch cultures for this purpose (51).

Salinity and δ^2H values of lake water were calculated by starting with the definition of the fractionation factor, α, as $(\delta^2H_{Lipid} + 1)/(\delta^2H_{Water} + 1)$. This was substituted into α − salinity regression equations for taraxerol and nC$_{24}$-alkanol:

$$m_{Tarax} * \text{salinity} + b_{Tarax} = (\delta^2H_{Tarax} + 1)/(\delta^2H_{Water} + 1),$$

$$m_{C24OL} * \text{salinity} + b_{C24OL} = (\delta^2H_{C24OL} + 1)/(\delta^2H_{Water} + 1),$$

where m_x and b_x are the respective slope and intercept values of the α-salinity relationships for each lipid, δ^2H_{Water} is the unknown δ^2H value of the lake water, and δ^2H_{Tarax} and δ^2H_{C24OL} are the values from the sediment biomarkers. The intercept value for each compound (b_x) was calculated using the definition of α and the modern δ^2H_{Water} value as described above. δ^2H_{Tarax} and δ^2H_{C24OL} were measured, leaving two equations with two unknowns, δ^2H_{Water} and salinity, which were solved for. δ^2H_{Water} values were also calculated using the δ^2H_{C24OL} data and salinity calibration using a diatom-based salinity reconstruction (25). Linear interpolation was used to map the higher temporally resolved signal onto the age scale of the lower temporally resolved signal for calculations that used two measurements that were not made on the same sediment sample, as was the case for all diatom-biomarker pairings. The continuous 2,000-y records shown in Fig. 4 were produced by splicing the δ^2H_{Tarax} and δ^2H_{C24OL}-based salinity and δ^2H_{Water} reconstructions with the diatom and δ^2H_{C24OL}-based salinity and δ^2H_{Water} reconstructions (splice point between 1140 and 1160 CE) as well as the measured lake-water data from 2008 CE. This approach was selected over an averaging procedure to minimize dampening variability in the records.

ACKNOWLEDGMENTS. We thank Kim Cobb for water isotope analyses, Weijian Zhou for ^{14}C dates, and Alistair Seddon for providing data; Orest Kawka, Josh Gregersen, Nemiah Ladd, Alyssa Atwood, and Julie Richey for useful discussions and advice; Ariel Townsend for assistance in the laboratory; Alyssa Atwood and Simon Haberle for assistance in the field; and the editors at PNAS and two anonymous reviewers for helpful comments. We thank the University of Washington School of Oceanography for funding the fieldwork, Parque Nacional Galápagos for sampling permission, and the Charles Darwin Foundation for facilitating the fieldwork. This material is based upon work supported by National Science Foundation Grants ESH-0639640 and EAR-1348396 and National Oceanic and Atmospheric Administration Grant NA08OAR4310685 (to J.P.S.).

1. Chiang JCH (2009) The tropics in paleoclimate. *Annu Rev Earth Planet Sci* 37:263–297.
2. Gen Li S-PX (2014) Tropical biases in CMIP5 multimodel ensemble: The excessive equatorial Pacific cold tongue and double ITCZ problems. *J Clim* 27:1765–1780.
3. Jha B, Hu Z-Z, Kumar A (2014) SST and ENSO variability and change simulated in historical experiments of CMIP5 models. *Clim Dyn* 42(7):2113–2124.
4. Atwood AR, Sachs JP (2014) Separating ITCZ- and ENSO-related rainfall changes in the Galápagos over the last 3 kyr using D/H ratios of multiple lipid biomarkers. *Earth Planet Sci Lett* 404:408–419.
5. Conroy JL, Overpeck JT, Cole JE, Shanahan TM, Steinitz-Kannan M (2008) Holocene changes in eastern tropical Pacific climate inferred from a Galápagos lake sediment record. *Quat Sci Rev* 27:1166–1180.
6. Riedinger MA, Steinitz-Kannan M, Last WM, Brenner M (2002) A ~6100 ^{14}C yr record of El Niño activity from the Galápagos Islands. *J Paleolimnol* 27:1–7.
7. Sachs JP, et al. (2009) Southward movement of the Pacific intertropical convergence zone AD 1400–1850. *Nat Geosci* 2:519–525.
8. Zhang Z, Leduc G, Sachs JP (2014) El Niño evolution during the Holocene revealed by a biomarker rain gauge in the Galápagos Islands. *Earth Planet Sci Lett* 404:420–434.
9. Haug GH, Hughen KA, Sigman DM, Peterson LC, Röhl U (2001) Southward migration of the intertropical convergence zone through the Holocene. *Science* 293(5533): 1304–1308.
10. Conroy JL, Cobb KM, Noone D (2013) Comparison of precipitation isotope variability across the tropical Pacific in observations and SWING2 model simulations. *J Geophys Res, D, Atmospheres* 118(11):5867–5892.
11. Gat JR (1996) Oxygen and hydrogen isotopes in the hydrologic cycle. *Annu Rev Earth Planet Sci* 24:225–262.
12. Sachse D, et al. (2012) Molecular paleohydrology: Interpreting the hydrogen-isotopic composition of lipid biomarkers from photosynthesizing organisms. *Annu Rev Earth Planetary Sci* 40:221–249.
13. Ladd SN, Sachs JP (2012) Inverse relationship between salinity and *n*-alkane δD values in the mangrove Avicennia marina. *Org Geochem* 48:25–36.
14. M'boule D, et al. (2014) Salinity dependent hydrogen isotope fractionation in alkenones produced by coastal and open ocean haptophyte algae. *Geochim Cosmochim Acta* 130:126–135.
15. Nelson DB, Sachs JP (2014) The influence of salinity on D/H fractionation in dinosterol and brassicasterol from globally distributed saline and hypersaline lakes. *Geochim Cosmochim Acta* 133:325–339.
16. Ladd SN, Sachs JP (2015) Influence of salinity on hydrogen isotope fractionation in *Rhizophora* mangroves from Micronesia. *Geochim Cosmochim Acta* 168:206–221.
17. Sinninghe Damste JS, et al. (2001) Novel intact glycolipids in sediments from an Antarctic lake (Ace Lake). *Org Geochem* 32(2):321–332.
18. Castañeda IS, Werne JP, Johnson TC, Powers LA (2011) Organic geochemical records from Lake Malawi (East Africa) of the last 700 years, part II: Biomarker evidence for recent changes in primary productivity. *Palaeogeogr Palaeoclimatol Palaeoecol* 303(1-4):140–154.
19. Versteegh GJM, et al. (2004) Taraxerol and Rhizophora pollen as proxies for tracking past mangrove ecosystems. *Geochim Cosmochim Acta* 68(3):411–422.
20. Volkman JK (2003) Sterols in microorganisms. *Appl Microbiol Biotechnol* 60(5): 495–506.
21. Sachs JP (2014) Hydrogen isotope signatures in the lipids of phytoplankton. *Treatise on Geochemistry*, eds Holland HD, Turekian KK (Elsevier, Oxford), 2nd Ed, pp 79–94.
22. Sachs JP, Kawka OE (2015) The influence of growth rate on 2H/1H fractionation in continuous cultures of the coccolithophorid Emiliania huxleyi and the diatom Thalassiosira pseudonana. *PLoS ONE* 10(11):e0141643.
23. Trueman M, d'Ozouville N (2010) Characterizing the Galapagos terrestrial climate in the face of global climate change. *Galapagos Res* 67:26–37.
24. Kahmen A, et al. (2013) Leaf water deuterium enrichment shapes leaf wax n-alkane dD values of angiosperm plants II: Observational evidence and global implications. *Geochim Cosmochim Acta* 111:50–63.
25. Seddon AWR, Froyd CA, Leng MJ, Milne GA, Willis KJ (2011) Ecosystem resilience and threshold response in the Galápagos coastal zone. *PLoS One* 6(7):e22376.
26. Carton JA, Giese BS (2008) A reanalysis of ocean climate using simple ocean data assimilation (SODA). *Mon Weather Rev* 136:2999–3017.
27. Xie S-P, Okumura Y, Miyama T, Timmermann A (2008) Influences of Atlantic climate change on the tropical Pacific via the Central American isthmus. *J Clim* 21:3914–3928.
28. McBirney AR, Williams H (1969) *Geology and Petrology of the Galapagos Islands* (Geological Society of America, Boulder, CO).
29. Geist D (1996) On the emergence and submergence of the Galapagos islands. *Noticas de Galapagos* 56:5–9.
30. Pryet A, et al. (2012) Quantification of cloud water interception along the windward slope of Santa Cruz Island, Galapagos (Ecuador). *Agric For Meteorol* 161:94–106.
31. Bird BW, et al. (2011) A 2,300-year-long annually resolved record of the South American summer monsoon from the Peruvian Andes. *Proc Natl Acad Sci USA* 108(21): 8583–8588.
32. Reuter J, et al. (2009) A new perspective on the hydroclimate variability in northern South America during the Little Ice Age. *Geophys Res Lett* 36(21):L21706.
33. Salvatteci R, et al. (2014) The response of the Peruvian Upwelling Ecosystem to centennial-scale global change during the last two millennia. *Clim Past* 10:715–731.
34. Broccoli AJ, Dahl KA, Stouffer RJ (2006) Response of the ITCZ to Northern Hemisphere cooling. *Geophys Res Lett* 33(1):L01702.
35. Frierson DMW, et al. (2013) Contribution of ocean overturning circulation to tropical rainfall peak in the Northern Hemisphere. *Nat Geosci* 6:940–944.
36. Mann ME, et al. (2008) Proxy-based reconstructions of hemispheric and global surface temperature variations over the past two millennia. *Proc Natl Acad Sci USA* 105(36): 13252–13257.
37. Oppo DW, Rosenthal Y, Linsley BK (2009) 2,000-year-long temperature and hydrology reconstructions from the Indo-Pacific warm pool. *Nature* 460(7259):1113–1116.
38. Cobb KM, et al. (2013) Highly variable El Niño-Southern Oscillation throughout the Holocene. *Science* 339(6115):67–70.
39. Carré M, et al. (2014) Holocene history of ENSO variance and asymmetry in the eastern tropical Pacific. *Science* 345(6200):1045–1048.
40. Brock F, Higham T, Ditchfield P, Ramsey CB (2010) Current pretreatment methods for AMS radiocarbon dating at the Oxford Radiocarbon Accelerator Unit (Orau). *Radiocarbon* 52(1):103–112.
41. Hogg AG, et al. (2013) Shcal13 Southern Hemisphere calibration, 0–50,000 years Cal BP. *Radiocarbon* 55(4):1889–1903.
42. Hua Q, Barbetti M, Rakowski AZ (2013) Atmospheric radiocarbon for the period 1950–2010. *Radiocarbon* 55(4):2059–2072.
43. Stuiver M, Reimer PJ (1993) Extended ^{14}C data base and revised CALIB 3.0 ^{14}C age calibration program. *Radiocarbon* 35(1):215–230.
44. Carlson RE, Fritsch FN (1985) Monotone piecewise bicubic interpolation. *SIAM J Numer Anal* 22(2):386–400.
45. Anchukaitis KJ, Tierney JE (2013) Identifying coherent spatiotemporal modes in time-uncertain proxy paleoclimate records. *Clim Dyn* 41:1291–1306.
46. Nelson DB, Sachs JP (2013) Concurrent purification of sterols, triterpenols and alkenones from sediments for hydrogen isotope analysis using high performance liquid chromatography. *Org Geochem* 64:19–28.
47. Polissar PJ, D'Andrea WJ (2014) Uncertainty in paleohydrologic reconstructions from molecular dD values. *Geochim Cosmochim Acta* 129:146–156.
48. Sachs JP, Schwab VF (2011) Hydrogen isotopes in dinosterol from the Chesapeake Bay estuary. *Geochim Cosmochim Acta* 75:444–459.
49. Sachse D, Sachs JP (2008) Inverse relationship between D/H fractionation in cyanobacterial lipids and salinity in Christmas Island saline ponds. *Geochim Cosmochim Acta* 72:793–806.
50. Schouten S, et al. (2006) The effect of temperature, salinity and growth rate on the stable hydrogen isotopic composition of long chain alkenones produced by *Emiliania huxleyi* and *Gephyrocapsa oceanica*. *Biogeosciences* 3:113–119.
51. Zhang Z, Sachs JP, Marchetti A (2009) Hydrogen isotope fractionation in freshwater and marine algae: II. Temperature and nitrogen limited growth rate effects. *Org Geochem* 40:428–439.
52. Seddon AWR, Froyd CA, Witkowski A, Willis KJ (2014) A quantitative framework for analysis of regime shifts in a Galápagos coastal lagoon. *Ecology* 95(11):3046–3055.
53. Craig H, Gordon LI (1965) *Deuterium and Oxygen 18 Variations in the Ocean and Marine Atmosphere*, ed Tongiogi E (Consiglio Nazionale delle Ricerche Laboratorio de Geologia Nucleare, Spoleto, Italy), pp 9–130.
54. Gonfiantini R (1986) Environmental isotopes in lake studies. *Handbook of Environmental Isotope Geochemistry, The Terrestrial Environment B*, eds Fritz P, Fontes JC (Elsevier, Amsterdam), Vol II, pp 113–168.
55. Dansgaard W (1964) Stable isotopes in precipitation. *Tellus* 16(4):436–468.
56. Majoube M (1971) Fractionnement en oxygene-18 et en deuterium entre l'eau et sa vapeur. *J Chim Phys* 10:1423.
57. Gibson JJ, Prepas EE, McEachern P (2002) Quantitative comparison of lake throughflow, residency, and catchment runoff using stable isotopes: Modelling and results from a regional survey of Boreal lakes. *J Hydrol (Amst)* 262(1-4):128–144.
58. Roeckner E, et al. (2006) Sensitivity of simulated climate to horizontal and vertical resolution in the ECHAM5 Atmosphere Model. *J Clim* 19:3771–3791.
59. IAEA/WMO (2015) Global network of isotopes in precipitation. The GNIP Database. Available at www-naweb.iaea.org/napc/ih/index.html.
60. Steinman BA, Rosenmeier MF, Abbott MB, Bain DJ (2010) The isotopic and hydrologic response of small, closed-basin lakes to climate forcing from predictive models: Application to paleoclimate studies in the upper Columbia River basin. *Limnol Oceanogr* 55(6):2231–2245.
61. Hua Q, Barbetti M (2004) Review of tropospheric bomb ^{14}C data for carbon cycle modeling and age calibration purposes. *Radiocarbon* 46(3):1273–1298.